Title

Electrochemical Reaction Mechanism of the MoS2 Electrode in a Lithium-Ion Cell Revealed by in Situ and Operando X-ray Absorption Spectroscopy

Journal

Nano Letters, 18(2)

ISSN

1530-6984

Authors

Zhang, Liang
Sun, Dan
Kang, Jun
et al.

Publication Date

2018-02-14

DOI

10.1021/acs.nanolett.7b05246

Peer reviewed

Electrochemical Reaction Mechanism of the MoS_2 electrode in a Lithium-Ion Cell revealed by *in situ* and *operando* X-ray Absorption Spectroscopy

Liang Zhang,[1,†] Dan Sun,[2,†] Jun Kang,[3] Jun Feng,[1] Hans Bechtel,[1] Lin-Wang Wang,[3] Elton J. Cairns,[2,4*]

Jinghua Guo[1,5*]

1. Advanced Light Source, Lawrence Berkeley National Laboratory, Berkeley, CA 94720, USA
2. Energy Storage and Distributed Resources Division, Lawrence Berkeley National Laboratory, Berkeley, CA 94720, USA
3. Material Sciences Division, Lawrence Berkeley National Laboratory, Berkeley, CA 94720, USA
4. Department of Chemical and Biomolecular Engineering, University of California, Berkeley, California 94720, USA
5. Department of Chemistry and Biochemistry, University of California, Santa Cruz, California 95064, USA

Abstract

As a typical transition metal dichalcogenide, MoS_2 offers numerous advantages for nanoelectronics and electrochemical energy storage due to its unique layered structure and tunable electronic properties. When used as the anode in lithium-ion cells, MoS_2 undergoes intercalation and conversion reactions in sequence upon lithiation, and the reversibility of the conversion reaction is an important but still controversial topic. Here, we clarify that the conversion reaction of MoS_2 is not reversible and the formed Li_2S is converted to sulfur in the first charge process. Li_2S/sulfur becomes the main redox couple in the subsequent cycles and is the main contributor to the reversible capacity. In addition, due to the insulating nature of both Li_2S and sulfur, a strong relaxation effect is observed during the cycling process. Our study clearly reveals the electrochemical lithiation/delithiation mechanism of MoS_2, which can facilitate the further development of high-performance MoS_2 based electrodes.

Transition metal dichalcogenides (TMDs) represent a family of layered materials with versatile electronic, optical, and chemical properties.[1-3] As one of the most interesting TMDs, molybdenum disulfide (MoS_2) has been extensively investigated in a variety of areas, such as nanoelectronics, electrocatalysis, and energy storage devices.[4-8] MoS_2 is composed of hexagonal layers of molybdenum atoms coordinated with six sulfur atoms and the interactions between sulfur layers are characterized as weak van der Waals interactions. This unique structure gives rise to an interlayer distance of approximately 0.62 nm compared to the 0.34 nm spacing of graphite, a structural analog that is the most common commercial lithium-ion battery (LIB) anode material. The large interlayer distance allows a fast diffusion of lithium without causing a significant volume expansion, which enables MoS_2 to be a promising alternative anode material for high capacity LIBs.[4,5,9] For example, MoS_2 based electrodes can deliver a high reversible capacity of ~1100 mAh/g at a rate 0.5 A/g, which is much higher than the theoretical capacity of 669 mAh/g for MoS_2 assuming a complete conversion reaction ($\begin{matrix} -¿ \rightarrow 2Li_2S+Mo \\ +¿+4e^{¿} \\ MoS_2+4Li^{¿} \end{matrix}$).[10] The specific capacity, rate performance and cycle life can be further improved by interfacial modifications and structural controls for MoS_2 based electrodes.[4,5,10-13]

The electrochemical lithiation reaction of the MoS_2 electrode in LIBs is represented as follows:[4,5]

$$\begin{matrix} -¿ \rightarrow Li_xMoS_2 \quad (1) \\ +¿+xe^{¿} \\ MoS_2+xLi^{¿} \end{matrix}$$

$$\begin{matrix} -¿ \rightarrow Li_2S+Mo \quad (2) \\ +¿+(4-x)e^{¿} \\ Li_xMoS_2+(4-x)Li^{¿} \end{matrix}$$

where x is in the range of $0 \le x \le 1$. Here, equation (1) describes the intercalation reaction and equation (2) describes the conversion reaction. It is generally believed that the intercalation reaction (1), which corresponds to the voltage plateau occurring at ~1.1 V vs Li/Li^+ during the first discharge, is fully

reversible with a phase transition from trigonal prismatic (2H) to octahedral (1T) after lithiation.[14-17] In contrast, the mechanism underpinning the conversion reaction of MoS_2 occurring at ~0.5 V is still not well understood, despite decades of effort and intensive recent interest. Specifically, the reversibility of the conversion reaction almost immediately encountered a controversy, which remains today.[10,18-28] For example, a number of previous reports favored the reversible conversion reaction sequence of the MoS_2 electrode,[20-22,29,30] while the other reports claimed that the discharge product of MoS_2 (i.e., Mo and Li_2S) cannot be converted to MoS_2 in the following charge process, which is probably related to the covalent properties of Li_2S and the inertness of metallic Mo.[10,23-28,31] Instead, Li_2S is oxidized to elemental sulfur at a higher charge potential and Li_2S/sulfur becomes the sole redox couple in the following cycling process, as demonstrated in equation (3). However, there is still no solid evidence to support this reaction path.

$$-¿ \leftrightarrow Li_2S \quad (3)$$
$$+¿ + 2e^{¿}$$
$$S + 2Li^{¿}$$

Considering the wide application of MoS_2 and the important influence of reaction path on the design of superior-performance MoS_2 based electrodes, a comprehensive understanding and persuasive clarification of the reaction mechanism of MoS_2 is required, in both fundamental studies and practical applications.

Herein, we have comprehensively investigated the electrochemical lithiation/delithiation mechanism of MoS_2 by combining electrochemical investigation, morphology characterization, *in situ* and *ex situ* S K-edge and Mo L-edge X-ray absorption spectroscopy (XAS), and density functional theory (DFT) calculations. By simply manipulating the scanning voltage ranges, we show that the intercalation reaction is reversible but with the presence of an ~0.7% tensile strain after the first cycle, which could be the main reason of the different electrochemical responses for the first and following cycles. For the conversion reaction, we provide solid evidence that this reaction is not reversible and the deep lithiation product Li_2S is converted to sulfur in the subsequent delithiation process. In addition, the contrast between *in situ* and *ex situ* XAS results provides valuable information about the reaction dynamics of MoS_2. We believe that these findings could have great influence in advancing the development of MoS_2 based electrodes for LIBs.

Methods

Cell preparation and electrochemical cycling

The MoS_2 electrodes were prepared by grinding a mixture containing the commercial MoS_2 active material (Sigma), carbon black (superP) and polyvinylidene fluoride (PVDF) (pure MoS_2: C: PVDF = 70:20:10, by weight) for 10 min, then dispersing the mixture in N-methyl-2-pyrrolidinone (NMP) to make a slurry with a concentration of 300 mg/mL and stirring for 4 h, coating the slurry onto a commercial copper foil and evaporating the solvent at room temperature inside of a glove box (filled with argon) and drying overnight. 1 M $LiPF_6$ in ethylene carbonate (EC)/Diethyl carbonate (DEC) (1:1, by volume) was used as electrolyte. CR2325 coin cells were assembled in an argon-filled glove box. The cell consisted of a fabricated MoS_2 electrode, a lithium metal foil electrode (99.98%, Cyprus Foote Mineral) and a porous polypropylene separator (Celgard 2400). The electrochemical performance of the cells was evaluated between 0.8 V and 3.0 V or 0.05 V and 3.0 V using a battery cycler (Arbin BT2000). The CV study was conducted using a Biologic electrochemical workstation at a scan rate of 0.05 mV/s.

Characterization

The structure of the cycled samples was investigated by an X-ray diffractometer (XRD, Bruker AXS D8 Discover GADDS microdiffractometer) with a Co Kα radiation source after the samples were protected by a Kapton film and a Raman spectrometer (Labram, ISA Groupe Horida) with a 532 nm laser at 2 mW power after the samples were sealed in a chamber with a glass window. The morphology of the cycled samples was examined by a field emission scanning electron microscope (FESEM, JEOL JSM-7500F) with elemental mapping using energy-dispersive X-ray spectroscopy (EDS, Oxford).

X-ray absorption spectroscopy measurements

The *in-situ* and *ex-situ* S K-edge and Mo L-edge XAS spectra were measured at beamline 5.3.1 and 10.3.2 at the Advanced Light Source, Lawrence Berkeley National Laboratory. The X-ray beam size is ~100 μm × 100 μm. The XAS spectra were collected in total fluorescence yield mode and calibrated using elemental sulfur spectra by setting the position of the white line to 2472.2 eV. All the XAS spectra were measured under constant helium flow in the sample chamber and acquired continuously during the discharge/charge processes. The *in situ* electrochemical cells were adapted from the CR2325 coin cells: a 2×1 mm^2 hole was drilled at the MoS_2 (positive) side of the cell housing using a high precision laser system; the hole was then sealed with a 13 μm thick Kapton film to avoid air exposure while allowing X-

ray beam penetration (the X-ray transmission ratio of a 13 μm thick Kapton film at 2470 eV is ~65%). In addition, we applied a copper mesh as the holder for the MoS_2 electrode materials to allow the direct detection of MoS_2 by incoming X-rays. The *ex-situ* sulfur L-edge XAS and XES spectra were measured at beamline 8.0.1.4 at the Advanced Light Source, Lawrence Berkeley National Laboratory.

Calculation details

DFT calculations were performed using the Vienna ab initio simulation package (VASP).[32] The projector-augmented wave method[33] was used to describe the core−valence interaction. To account for the effect of van der Waals interaction, the optB86b-vdW functional was adopted as the exchange-correlation functional.[34] The wave functions are expanded in a plane-wave basis set with a 400 eV cutoff. All atoms are allowed to relax until the calculated force on each atom is smaller than 0.01 eV/Å.

Results

Electrochemical performance. We firstly investigated the electrochemical performance of the MoS_2 electrode in the voltage range of 0.8-3.0 V and 0.05-3.0 V versus Li/Li^+ at a current density of 0.2 A/g, where the intercalation reaction should occur for the former and both intercalation and conversion reactions should take place for the latter.[4,5] Figure 1a shows the representative galvanostatic lithiation (discharge) /charge (delithiation) voltage between 0.8 and 3.0 V. One voltage plateau located at 1.0 V can be well observed in the first discharge, which corresponds to the formation of Li_xMoS_2 $(0 \le x \le 1)$ by the intercalation of lithium into pristine MoS_2. The initial discharge and charge capacities are 239 and 162 mAh/g, respectively, corresponding to a Coulombic efficiency (CE) of 67.8% (Figure 1b). The relatively low initial CE could be related to some irreversible processes during the first cycle. The voltage profiles of the following discharges become different from that of the first discharge, where two plateaus at higher voltages are clear. In contrast, the plateaus in the charge voltage profiles are symmetric to that in the discharge voltage profiles, suggesting that the electrochemical reactions are highly stable and reversible in the electrode after the initial cycle. This is consistent with the excellent cycling performance of the MoS_2 electrode: the reversible capacity is still maintained at 135 mAh/g after 100 cycles with a high CE of nearly 100%.

To further understand the lithium storage mechanism, cyclic voltammetry (CV) of MoS_2 was performed for 5 cycles at a scan rate of 0.05 mV/s by sweeping between 0.8 and 3.0 V, and the corresponding results are shown in Figure 1c. The pronounced reduction peak at ~1.0 V in first cathodic scan is related to the formation of $LiMoS_2$. The split of the feature indicates a multistep lithium intercalation mechanism.[11,25] In the subsequent cathodic scans, the peak gradually shifts to higher potentials with decreased intensity, which is likely due to the consumption of the active materials. [4] In addition, two cathodic peaks with continuously increased intensities appear at 1.9 and 2.5 V from the second cycles, which implies a different electrochemical response after the first cycle.[4,25] The three peaks at 1.9, 2.0, and 2.5 V in the anodic scans indicate the multistep delithiation process.[26]

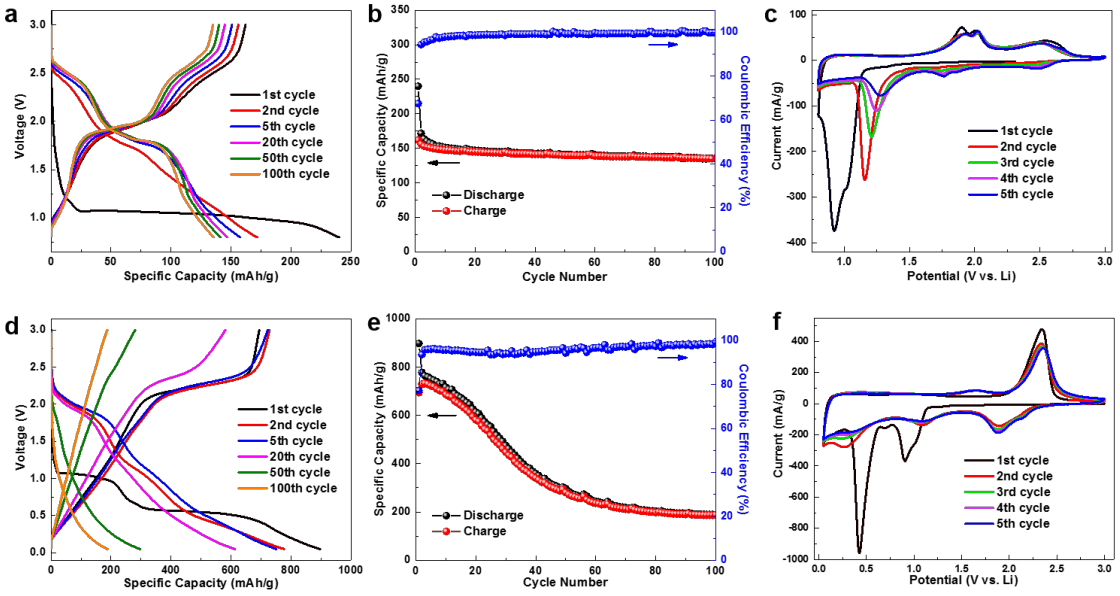

Figure 1. Electrochemical characterization of the electrodes with different discharge cut-off voltages. (a) Discharge/charge voltage profiles, (b) cycling performance and Coulombic efficiency, and (c) cyclic voltammograms of MoS_2 electrode with a discharge cut-off voltage of 0.8 V. (d) Discharge/charge voltage profiles, (e) cycling performance and Coulombic efficiency, and (f) cyclic voltammograms of MoS_2 electrode with a discharge cut-off voltage of 0.05 V.

By decreasing the discharge cut-off voltage to 0.05 V, a conversion reaction at lower voltage (~0.5 V) following the above-mentioned intercalation reaction is clear in the first discharge (Figure 1d). The reversible capacity of the first cycle is 694 mAh/g, which is a little higher than the assumed theoretical

capacity of 669 mAh/g. The higher capacity was proposed to be related to the intrinsic charge storage capacity of the carbon material used as conductive additive in the electrode.[4,35] The high irreversible capacity of 200 mAh/g in the first cycle (corresponding to a CE of 77.4%) could be related to electrolyte decomposition at low potentials and the pulverization of the active materials.[10,25] During the subsequent discharge cycles, the plateaus observed at ~1.0 and 0.5 V simultaneously disappear with the emergence of two new inconspicuous plateaus at ~1.1 and 1.9 V, which is consistent with previous observations.[9,12,23] In the charge process, a plateau at 2.3 V is well discerned. However, after 50 cycles the plateaus in both discharge and charge processes disappear, resulting in a rapid decay of the specific capacity to only 180 mAh/g after 100 cycles (Figure 1 e). Note that the focus of present study is to understand the lithiation/delithiation mechanism of the MoS_2 electrode rather than to improve its cycling performance. The CV results shown in Figure 1f confirm that both the 1.0 and 0.5 V plateaus, which correspond to the intercalation interaction (1) and conversion reaction (2), respectively, are only observed in the first cathodic scan, implying that an irreversible phase transformation of MoS_2 is likely. The weak but discernable feature at ~0.3 V in the following cathodic scans is related to the conversion reaction of the remaining MoS_2 in the electrode. Moreover, the CV curves after the first cathodic scan become similar to those of a Li/S cell (supplementary Figure 1), probably indicating that the pertinent redox reaction involves lithium and sulfur as the electroactive species in the following cycles.[4,26] Note that the weak redox couple at ~1.1 V in the cathodic scan and ~1.7 V in anodic scan may be related to intermediate polysulfides as they are only observed from the second cycle.

Morphology and structure characterization of cycled MoS_2 electrodes. We next characterized the morphology evolution of MoS_2 at different states of charge by scanning electron microscopy (SEM). The pristine MoS_2 and as prepared MoS_2 electrode show the typical flake structure with a lateral size ranging from tens to hundreds of nm (Figure 2a and b). This typical structure is clearly demonstrated for MoS_2 discharged to 0.8 V (Figure 2c) and charged back to 3.0 V (Figure 2d). Actually, the MoS_2 still maintains the well-distinguished flake structure even after 10 cycles (Supplementary Figure 2a-c), implying the relatively high reversibility of lithium intercalation/deintercalation for MoS_2. This is also confirmed by the fact that a high specific capacity (~750 mAh/g) is still achieved with a deeper discharge to 0.05 V after 100 cycles in the voltage rang of 0.8-3.0 V (Supplementary Figure 3).

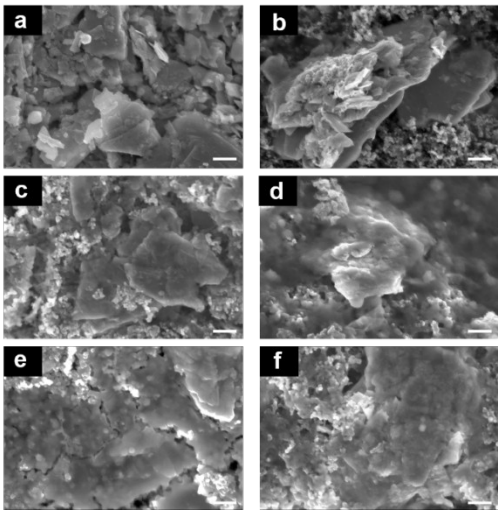

Figure 2. Morphology characterization of pristine and cycled MoS_2 electrodes. SEM images of MoS_2 flakes (a), pristine MoS_2 electrode (b), MoS_2 discharge to 0.8 V (c), MoS_2 charge to 3.0 V after discharge to 0.8 V (d), MoS_2 discharged to 0.05 V (e), and MoS_2 charged to 3.0 V after discharge to 0.05 V (f). Scale bars, 200 nm.

In comparison, for MoS_2 discharged to 0.05 V (Figure 2e) and charged back to 3.0 V (Figure 2f), the flake structure disappears probably due to the irreversible conversion of MoS_2 to Li_2S and Mo, and instead a polymer/gel-like solid-electrolyte interface (SEI) film forms on the electrode surface, resulting in the increase of the content of carbon and oxygen species in the electrodes (Supplementary Figures 4 and 5). The thickness of this film continuously increases with further cycling, and a porous and mossy film is clearly visible after 10 cycles (Supplementary Figure 2d-f). Therefore, the observed fast capacity fading in a voltage window of 0.05-3.0 V could be related to an undesired side reaction at low potentials (below 0.6 V): the volume expansion of the lithiation products with partial damage of the formed SEI film and the rapid depletion of electrolyte with a continuous growth of the SEI film.[4]

To address the phase evolution during lithium insertion/extraction, *ex situ* X-ray diffraction (XRD) analysis for MoS_2 at different potentials was carried out (Figure 3a). For pristine MoS_2, all diffraction peaks can be indexed to the 2H phase of MoS_2 ($P6_3/mmc$, PDF no. 37-1492). When discharged to 0.8 V, most of the characteristic peaks of MoS_2 shift to lower angles. This observation is consistent with the expansion of the d-spacing of the MoS_2 structure due to lithium intercalation, as shown in equation (1), which induces a

distortion of the entire hexagonal crystal symmetry and causes a crystal structure transformation from 2H to the 1T phase.[36] The appearance of new diffraction peaks at 23.5° and 32.5° could also be related to the phase transformation. Upon recharging the electrode to 3.0 V, some representive diffraction peaks move towards higher angles, but their positions are still lower than those of pristine MoS_2 (Supplementary Figure 6) due to the remaining lithium trapped in MoS_2. This can also explain the low CE in the initial cycle shown in Figure 1b.

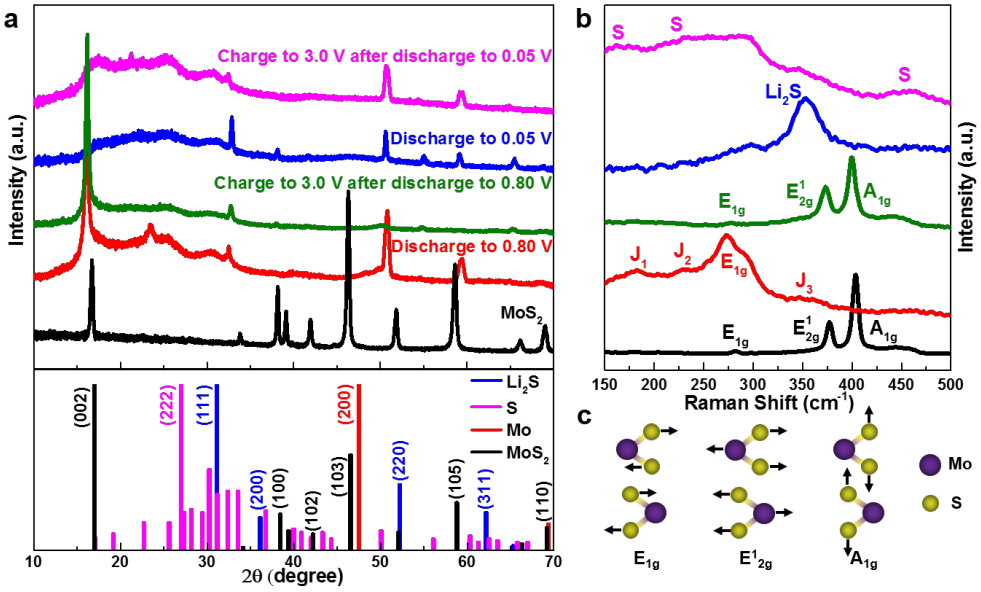

Figure 3. Structure characterization of pristine and cycled MoS_2 electrodes. (a) *Ex-situ* XRD patterns of MoS_2 electrodes at different cycling stages as labelled. Also shown are the reference patterns of Li_2S (PDF no. 23-0369), S (PDF no. 42-1278), Mo (PDF no. 42-1120), and MoS_2 (PDF no. 37-1492). (b) *Ex-situ* Raman spectra of MoS_2 electrodes at different cycling stages. (c) Atomic vibration direction of different Raman modes of MoS_2.

In contrast, if the electrode is discharged to 0.05 V, the representive reflection patterns of MoS_2 either totally vanish or become much weaker, while the characteristic reflection patterns of Li_2S appear at 32.9°, 38.1°, 54.9°, and 65.5°, respectively. However, no diffraction feature related to metallic Mo is observed, suggesting that the produced metallic Mo is in a small cluster form.[37] The formation of metal nanoparticles has also been observed for other conversion electrodes in LIBs, e.g., FeF_2,[38] NiO,[39] and CoO.[40] When charged back to 3.0 V, the intensity of the Li_2S related features is significantly decreased while the

diffraction peaks related to MoS_2, especially the diffraction peak for the (002) plane, are not recovered, which indicates that Li_2S is not transformed back to MoS_2 but more likely is converted to sulfur (equation (3)). The absence of sulfur related diffraction peaks indicates that the formed sulfur is amorphous.[25,26,28,41]

To validate the XRD results, we further carried out *ex situ* Raman analysis for the same samples (Figure 3b and supplementary Figure 6). The advantage of Raman spectroscopy is that it is capable of characterizing species that are amorphous or crystalline as it detects vibrational, rotational and other low-frequency modes of the investigated system. For the pristine MoS_2 electrode, the three peaks located at 281.2, 377.2, and 403.5cm^{-1} are assigned to E_{1g}, E^1_{2g}, and A_{1g} vibrational modes of 2H-MoS_2, respectively.[6,42] These signatures disappear for the MoS_2 electrode discharged to 0.8 V, and accordingly four new broad peaks occur at 181.3, 228.5, 273.1, and 350.1 cm^{-1}, which are attributed respectively to the J_1, J_2, E_{1g}, and J_3 vibrational modes of 1T-MoS_2.[42,43] These results clearly indicate the 2H to 1T phase transition for MoS_2 after discharge to 0.8 V. Charging MoS_2 to 3.0 V results in the restoration of E^1_{2g} and A_{1g} modes with lower frequencies compared with that of pristine MoS_2 (373.6 cm^{-1} vs. 377.2 cm^{-1} for E^1_{2g} mode and 400.1 cm^{-1} vs. 403.5 cm^{-1} for A_{1g} mode). As the E^1_{2g} and A_{1g} modes are highly sensitive to tensile or compressive strain in MoS_2, the red-shift of ~3.4 cm^{-1} for A_{1g} mode indicates the presence of an ~0.7% tensile strain in charged MoS_2.[9,44,45] The presence of tensile train in MoS_2 after the first cycle is expected to significantly impact the electrochemical process of MoS_2,[3] which could be the main reason for the different electrochemical voltage profiles of the first and following cycles shown in Figure 1a and c. For MoS_2 with a deep discharge to 0.05 V, a distinct Raman peak at 355.2 cm^{-1} is observed due to the formation of Li_2S (supplementary Figure 6), consistent with the XRD results. When the electrode is charged to 3.0 V, peaks related to elemental sulfur are observed accompanied with a significant decrease of the Li_2S feature. This confirms that the conversion reaction shown in equation (2) is not reversible and the reaction product Li_2S is converted to sulfur following equation (3), which is in good agreement with the electrochemical characterizations and XRD results.

***In situ* and *ex situ* XAS of MoS_2 electrodes in the voltage range of 0.8-3.0 V.** To better reveal the electrochemical reaction mechanism of MoS_2, we have further performed *in situ* and *ex situ* XAS at the sulfur K-edge and Mo L-edge to evaluate the electronic and chemical evolution of the active species during the charge/discharge process. Figure 4a and b show the *in situ* and *operando* sulfur K-edge XAS maps

(XAS intensity displayed as a function of photon energy and specific capacity) accompanied with the corresponding voltage profiles during the first discharge and charge, respectively. The main feature located at ~2471.5 accompanied with a shoulder at higher energy side reflects the sulfur 3p orbitals antibonding with Mo 4d states (such hybridization feature is also observed in sulfur L-edge XAS, see supplementary Figure 7).[46] The broad feature at ~2480.5 eV is induced by the hybridization between sulfur 3p orbitals and Mo 5s and 5p orbitals, which constitutes a kind of continuum states.

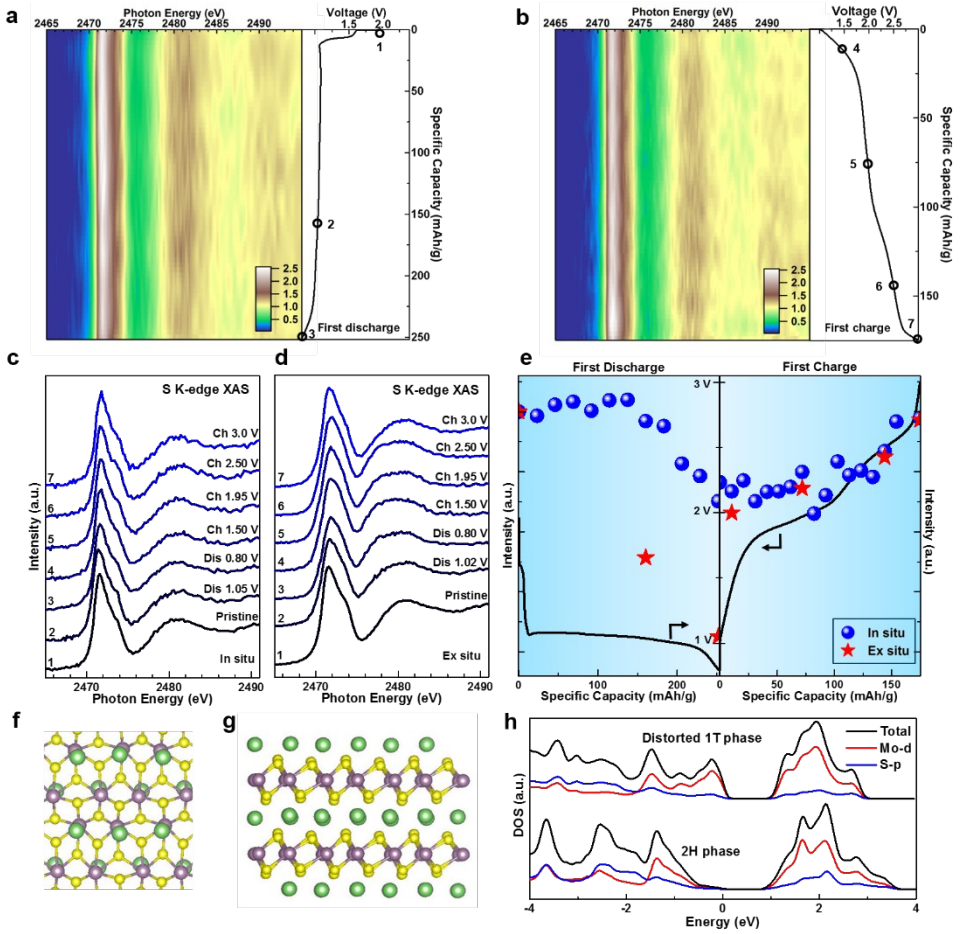

Figure 4. *In situ* and *Ex situ* XAS of MoS_2 electrodes in the voltage range of 0.8-3.0 V. (a and b) *In situ and operando* sulfur K-edge XAS mapping and the corresponding voltage profile for the first discharge and first charge, respectively. (c), (d) Representive *in situ* and *operando* (c) and *ex situ* (d) sulfur K-edge XAS spectra at different discharge/charge states as marked in (a) and (b). (e) Intensity evolution of MoS_2 as a function of specific capacity derived from *in situ* and *ex situ* XAS results. (f), (g) Top view and side view of

the calculated structure of $LiMoS_2$. (h) Calculated density of states of 2H-MoS_2 and distorted 1T-$LiMoS_2$. The energy of the valence band maximum is set to zero.

During the first cycle, no obvious change is observed for the XAS mapping results. This can be seen more clearly from the representive *in situ* spectra shown in Figure 4c: both the spectral shape and the peak position are nearly constant for the XAS spectra at different charge states. A similar phenomenon is also observed for the corresponding *ex situ* XAS spectra at the same discharge and charge states (Figure 4d and supplementary Figure 8). To visualize more clearly how the *in situ* and *ex situ* XAS spectra are developed, we have plotted the intensity of the main feature of MoS_2 at 2471.5 eV as a function of specific capacity (Figure 4e). Note that the derived values were normalized by the maximum value to directly compare the *in situ* and *ex situ* results. The intensity obtained from *in situ* and *operando* XAS shows a weak function of capacity initially and decreases continuously afterward during the first discharge, while the intensity gradually recovers during the subsequent charge, corresponding to the transformation from MoS_2 to $LiMoS_2$ and then back to MoS_2.[25,35] Similarly, the intensity derived from *ex situ* XAS demonstrates the same trend but with a larger intensity decrease at the end of the first discharge, indicating a higher lithium intercalation extent.

To better understand the intensity evolution, we have calculated the structure of $LiMoS_2$, as demonstrated in Figure 4f (top view) and g (side view). We identify that the tetrahedral sites on top of Mo atoms are the preferred lithium sites. In addition, the intercalated lithium induces a structural transition from the trigonal 2H phase to the octahedral 1T phase, in good agreement with the XRD and Raman results.[47,48] Moreover, the charge transfer from lithium to MoS_2 also results in a structural distortion of the 1T phase (Figure 4f and g and supplementary Figure 9), which contributes to the reduction of the total system energy through the Peierls distortion mechanism. It is very likely that the electrons transferred from lithium are located on not only the Mo 4d orbitals but also the S 3p orbitals, resulting in a slight intensity decrease of unoccupied S 3p states in the discharge process (Figure 4e).[49] This is consistent with the Mo L-edge XAS results (2p to 4d transition) that show no noticeable shift of Mo 4d states at different charge and discharge states (supplementary Figures 10 and 11), confirming that the electrons transferred from lithium are only partially located on Mo 4d orbitals and the valence state of Mo in $LiMoS_2$ is not +3 but $+(3+\delta)$ ($0<\delta<1$). For pristine MoS_2, the 2H phase is semiconducting with a bandgap of ~1.0 eV (Figure 4h) and the corresponding 1T

phase exhibits a metallic character.[47,48] However, the analysis of density of states discloses that the distorted 1T-MoS_2 is also semiconducting with a similar band gap as that of 2H-MoS_2 (Figure 4h), which could result in a sluggish electrochemical kinetics and thus the extent of lithium intercalation. This explains the relatively small intensity decrease at the end of the first discharge for *in situ* XAS results compared with the *ex situ* XAS results: the MoS_2 electrode is in a non-equilibrium state due to the kinetic effect of lithium intercalation for the former, while it is in an equilibrium state owing to enough relaxation time for the latter. Note that at the end of the first charge the intensities obtained from both *in situ* and *ex situ* XAS are lower than the corresponding values before cycling, probably highlighting the remaining lithium ions trapped at the defect states and/or grain boundaries of MoS_2. This provides a picture consistent with the Raman results that it is the residual lithium at the end of the first charge that results in different electrochemical voltage profiles between the first and following cycles. In addition, the *in situ* and *operando* sulfur K-edge and Mo L-edge XAS spectra of the second cycle demonstrate the same behavior as that of the first cycle (supplementary Figures 12 and 13), which again demonstrates the high reversibility of the intercalation reaction shown in equation (1).

***In situ* and *ex situ* XAS of MoS_2 electrodes in the voltage range of 0.05-3.0 V.** If the discharge cut-off voltage is set to 0.05 V, the spectral shape of sulfur K-edge and Mo L-edge XAS spectra changes significantly during the cycling process. Figure 5a and b show the *in situ* and *operando* sulfur K-edge XAS maps and the corresponding voltage profiles during the first discharge and charge processes, respectively. A continuous decrease of the characteristic feature of MoS_2 followed by an emergence of a broad feature located at ~2476.4 eV is observed during the first discharge. This evolution is further evidenced by the representive *in situ* and *ex situ* sulfur K-edge XAS spectra shown in Figure 5c and d (the spectra of elemental sulfur and Li_2S are also shown as a fingerprint to assign the reaction products of MoS_2 at different charge states): the intensity of the MoS_2 peak undergoes a gradual decrease with discharge and two broad features located at ~2473.4 and ~2476.4 eV are gradually formed in the spectra, which clearly indicates the formation of Li_2S.[50,51] The formation of Li_2S is more apparent in the *ex situ* XAS result shown in Figure 5d. The *ex situ* XAS spectrum for MoS_2 discharged to 0.3 V shows a similar spectral shape as that of the Li_2S reference material and no spectral shape change is discernable with further discharge to 0.05 V. In addition, both the *in situ* and *ex situ* Mo L-edge XAS results (supplementary Figures 10 and 14)

demonstrate a gradual shift of the main peak from 2524.6 to 2524.0 eV, indicative of the formation of metallic Mo at the end of the first discharge. These results indicate that, on the one hand, MoS_2 is continuously converted to Li_2S and Mo following equation (2) during discharge, and on the other hand, the conversion reaction is complete before 0.3 V and the capacity below 0.3 V can be largely attributed to formation of an SEI layer arising due to electrolyte decomposition.[4]

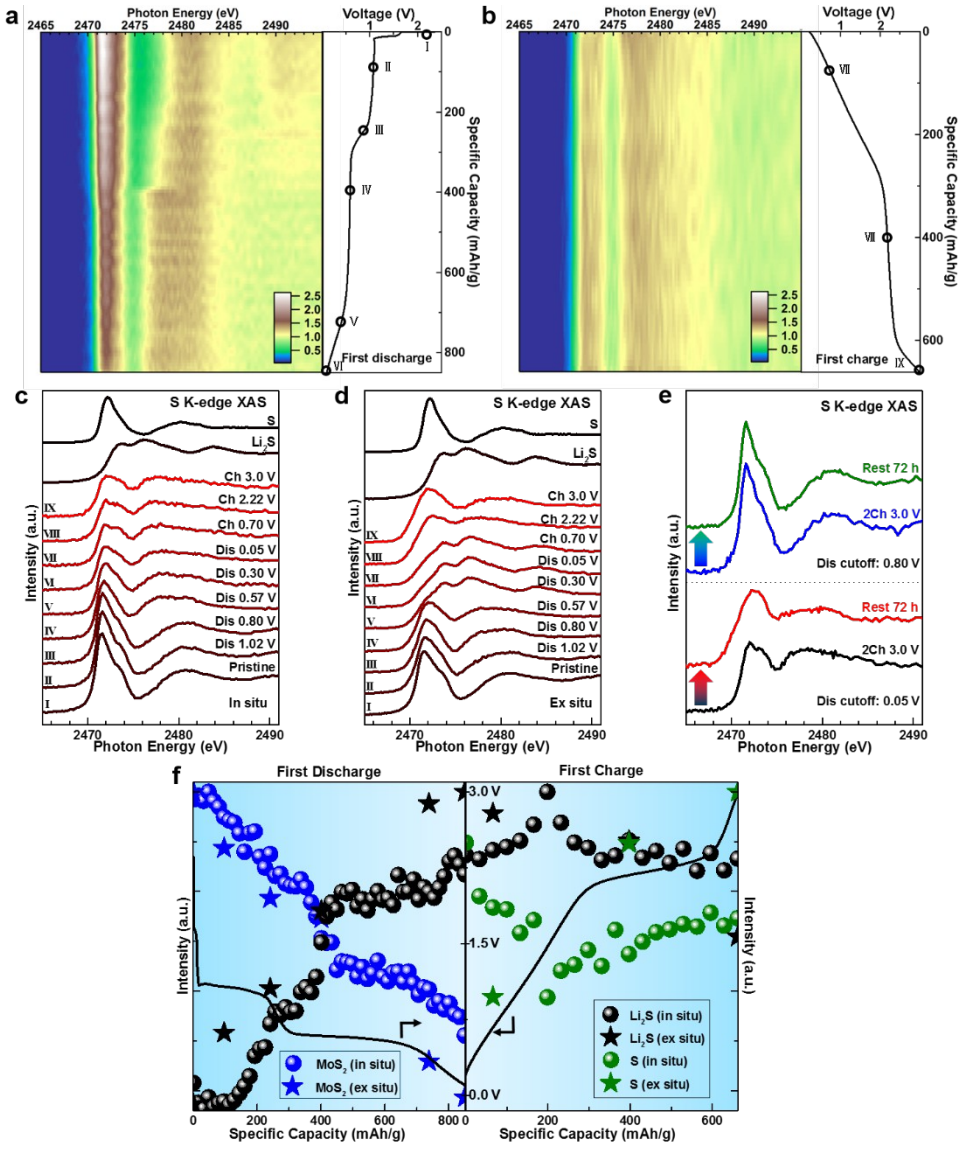

Figure 5. *In situ* and *Ex situ* XAS of MoS_2 electrodes in the voltage range of 0.05-3.0 V. (a), (b) *In situ and operando* sulfur K-edge XAS mapping and the corresponding voltage profile for the first discharge and first charge, respectively. (c), (d) Representive *in situ and operando* (c) and *ex situ* (d) sulfur K-edge XAS

spectra at different discharge/charge stages as marked in (a) and (b). (e) Sulfur K-edge XAS spectra of cycled MoS_2 electrodes before and after 72h of relaxation. (f) Intensity evolution of different species as a function of specific capacity derived from *in situ* and *ex situ* XAS results.

Interestingly, the fingerprint feature of MoS_2 in the sulfur K-edge XAS (Figure 5b, c and d, and supplementary Figure 15) is not recovered in the following charge and discharge processes, strongly indicating the irreversibility of the conversion reaction of equation (2). Instead, a feature at ~2472.2 eV, which is close to that of elemental sulfur, starts to emerge and then becomes dominant during the first charge, indicating the conversion from Li_2S to sulfur. However, the XAS spectra at the end of the first charge (Figure 5c and d) are quite broader compared with the spectrum of elemental sulfur, suggesting the amorphous nature of the formed sulfur product as revealed by XRD. Moreover, during the following charge and discharge processes, the Mo peak in Mo L-edge XAS (supplementary Figures 10, 14 and 16) is stabilized at 2524.0 eV (it should be at 2524.6 eV for MoS_2), which strongly suggests that the metallic Mo does not participate in the subsequent electrochemical reaction.

Of note, it seems that the lithiation/delithiation level derived from *in situ* results is always lower than that of *ex situ* results by comparing the corresponding XAS spectra shown in Figure 5c and d. To rule out the possibility that the material inside the X-ray detection area of the MoS_2 electrode is inactive, we left the cell at the charged state after 2 cycles under open-circuit. As shown in Figure 5e, after a relaxation of 72 h without further charging, the spectrum displays a shape similar to that of the *ex situ* XAS result at the same charge state (spectrum IX in Figure 5d). This observation indicates that the material in the detection area of the *in situ* cell is active but with a slow response to the electrochemical process. Such a relaxation effect could be related to the insulating properties of both sulfur and Li_2S.[52,53] In contrast, no such relaxation effect is observed for the same electrode with a discharge cut-off voltage of 0.8 V (Figure 5e) because of the relatively higher conductivity of MoS_2 and $LiMoS_2$.

To further understand the spectral response to the electrochemical process, we have also qualitatively investigated the intensity evolution of MoS_2 and different reaction products as a function of specific capacity for both *in situ* and *ex situ* XAS spectra (Figure 5f). Note that the derived values are normalized by the maximum value for MoS_2 and Li_2S and the minimum value for sulfur to directly compare the *in situ* and

ex situ results. A gradual intensity decrease is observed for MoS_2 during the first discharge, which is expected considering the conversion from MoS_2 to Li_2S. Accordingly, the intensity of Li_2S gradually increases during discharge. However, the intensity of Li_2S still increases at the initial charge process and reaches the maximum at a charge voltage of ~1.2 V, indicating the conversion reaction also occurs at the beginning of the charge process. This observation implies that the electrode materials can still react with local electrons and lithium ions to form Li_2S at low charge voltages, which is probably related to the sluggish kinetics of the formation of Li_2S.[52,53] In the remaining charge process, the intensity of Li_2S decreases as a consequence of transformation from Li_2S to sulfur, leading to the intensity increase of sulfur. Note that the initial decrease of sulfur content does not really reflect the intensity evolution of sulfur but MoS_2, because the peak position of sulfur (2472.2 eV) is very close to that of MoS_2 and $LiMoS_2$ (2471.5 eV). Actually, at such low potentials the formed Li_2S is not electrochemically active as merely capacitive current is observed in the CV results (Figure 1c) and thus the formation of sulfur is not exptected.[52,53] Here, it is worth mentioning that the intensity evolution of *in situ* results is always retarded compared with that of *ex situ* results, mainly due to the relaxation effect discussed above.

For Li/S cells, the intermediate polysulfides formed during cycling have a high solubility in organic electrolytes, which causes the shuttle effect.[52,53] The formation and dissolution of polysulfides in Li/S cells is shown in Figure 6a. The DEC solution containing a cycled sulfur electrode demonstrates a typical yellow-gold color of polysulfides. In contrast, for MoS_2 electrodes at fully-discharged (0.05 V) and fully-charged (3.0 V) states of different cycles, all the DEC solutions are still colorless, indicating almost negligible dissolution of polysulfides. The absence of the polysulfide formation during cycling is excluded as the CV results clearly show two reduction peaks at 2.2 and 1.9 V, corresponding to the stepwise reduction of elemental sulfur to polysulfides and further to Li_2S. We speculate that there are two possibilities accounting for the confinement of intermediate polysulfides. This first is that the formed Mo nanoparticles could serve as pinning sites for intermediate polysulfides and thus help to prevent their dissolution.[25,28,37] The first-principle simulations (supplementary Figure 17) also indicate that there exist strong binding strengths between Mo metal nanoparticles and polysulfides with different orders. The second is that the limited amount of unreacted MoS_2 in the electrode may also provide strong anchoring sties towards the intermediate polysulfides.[54] To validate this possibility, we also performed the polysulfide

adsorption test to provide detailed information on the interaction between polysulfides and MoS_2 (supplementary Figure 18). The result clearly indicates that the originally yellow-gold polysulfide solution becomes colorless after the addition of MoS_2, indiating a strong interaction between MoS_2 and polysulfides. However, the exact cause for the mitigation of the polysulfide dissolution is not yet fully understood, and further investigation is highly recommended.

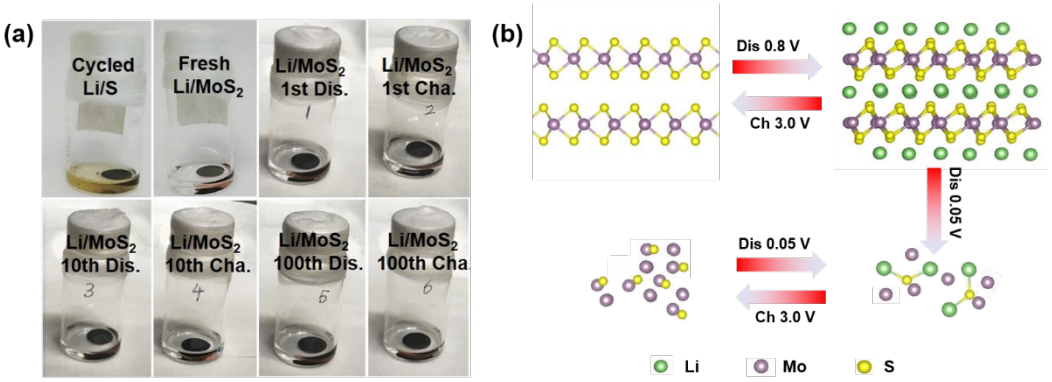

Figure 6. Dissolution of polysulfides for cycled MoS_2 electrodes. (a) Digital image of the dissolution of polysulfides in DEC solution for Li/MoS_2 cells at fully-discharged (0.05 V) and fully-charged (3.0 V) states of different cycles. For comparison, the corresponding result for cycled Li/S cell is also shown. (b) The proposed electrochemical reaction mechanism of MoS_2 electrode.

Conclusions

In summary, we have comprehensively studied the electrochemical reaction mechanism of the MoS_2 electrode in lithium cells by a combined experimental and theoretical investigation. As summarized in Figure 6b, the intercalation reaction of MoS_2 is reversible, accompanied with a phase transformation between 2H and distorted 1T phases. Both phases have a semiconducting character, which leads to slightly sluggish electrochemical kinetics. The remaining lithium at the end of first charge induces an ~0.7% tensile strain in MoS_2, resulting in the distinct electrochemical voltage profiles for the first and following cycles. In contrast, the conversion reaction is irreversible and the discharge product Li_2S is oxidized to sulfur in the first charge, clarifying the previous debate about the reversibility of the conversion reaction of MoS_2. As a consequence, the electrode behaves like a sulfur electrode after the first cycle, which mainly contributes to the reversible capacity in the subsequent cycles. Because both Li_2S and sulfur are insulators, a strong

relaxation effect is observed during cycling. In addition, we observed that the cycled MoS_2 electrode can strongly immobilize the intermediate polysulfides and therefore suppress the “shuttle effect” in Li/S cells, which may due to the adsorption property of remaining layered MoS_2 after lithium insertion toward polysulfides and also the as-formed Mo nanoparticles may further catalyze the conversion of polysulfides, however, further theoretical calculations and experiments are required to validate our assumptions. This research enriches the fundamental understanding of the electrochemical reaction mechanism of the MoS_2 electrode, which is a crucial step toward the rational design of layered TMD electrodes with superior cycling stability and electrochemical performance. In addition, the application of the *in situ* and *operando* XAS can also be extended for studying other TMD electrodes in both lithium-ion and sodium-ion cells.

Acknowledgement
The work at Advanced Light Source and Molecular Foundry of the Lawrence Berkeley National Laboratory were supported by the Director, Office of Science, Office of Basic Energy Sciences, of the U.S. Department of Energy under Contract No. DE-AC02-05CH11231. Work in the Energy Technologies Area of Lawrence Berkeley National Laboratory was supported by CERDEC U.S. ARMY under project No.104302.

References

1. D. Voiry, A. Mohite and M. Chhowalla, *Chem Soc Rev*, 2015, **44**, 2702-2712.
2. C. Tan, X. Cao, X. J. Wu, Q. He, J. Yang, X. Zhang, J. Chen, W. Zhao, S. Han, G. H. Nam, M. Sindoro and H. Zhang, *Chem Rev*, 2017, DOI: 10.1021/acs.chemrev.6b00558.
3. H. D. Yoo, Y. Liang, H. Dong, J. Lin, H. Wang, Y. Liu, L. Ma, T. Wu, Y. Li, Q. Ru, Y. Jing, Q. An, W. Zhou, J. Guo, J. Lu, S. T. Pantelides, X. Qian and Y. Yao, *Nat Commun*, 2017, **8**, 339.
4. T. Stephenson, Z. Li, B. Olsen and D. Mitlin, *Energy Environ. Sci.*, 2014, **7**, 209-231.
5. T. Wang, S. Chen, H. Pang, H. Xue and Y. Yu, *Advanced science*, 2017, **4**, 1600289.
6. H. Wang, Z. Lu, S. Xu, D. Kong, J. J. Cha, G. Zheng, P. C. Hsu, K. Yan, D. Bradshaw, F. B. Prinz and Y. Cui, *Proc Natl Acad Sci U S A*, 2013, **110**, 19701-19706.
7. B. Radisavljevic, A. Radenovic, J. Brivio, i. V. Giacometti and A. Kis, *Nature nanotechnology*, 2011, **6**, 147-150.
8. X. Zhang, Z. Lai, C. Tan and H. Zhang, *Angew Chem Int Ed Engl*, 2016, **55**, 8816-8838.
9. L. Oakes, R. Carter, T. Hanken, A. P. Cohn, K. Share, B. Schmidt and C. L. Pint, *Nat Commun*, 2016, **7**, 11796.
10. Y. Wang, L. Yu and X. W. Lou, *Angew Chem Int Ed Engl*, 2016, **55**, 7423-7426.
11. S. Wang, B. Y. Guan, L. Yu and X. W. D. Lou, *Advanced materials*, 2017, **29**.
12. C. Zhu, X. Mu, P. A. van Aken, Y. Yu and J. Maier, *Angew Chem Int Ed Engl*, 2014, **53**, 2152-2156.
13. H. Hwang, H. Kim and J. Cho, *Nano Lett*, 2011, **11**, 4826-4830.

14. E. Benavente, M. Santa Ana, F. Mendizábal and G. González, *Coordination chemistry reviews*, 2002, **224**, 87-109.
15. M. Azhagurajan, T. Kajita, T. Itoh, Y. G. Kim and K. Itaya, *Journal of the American Chemical Society*, 2016, **138**, 3355-3361.
16. L. Wang, Z. Xu, W. Wang and X. Bai, *Journal of the American Chemical Society*, 2014, **136**, 6693-6697.
17. Z. Zeng, X. Zhang, K. Bustillo, K. Niu, C. Gammer, J. Xu and H. Zheng, *Nano Lett*, 2015, **15**, 5214-5220.
18. M. S. Whittingham and F. R. Gamble, *Materials Research Bulletin*, 1975, **10**, 363-371.
19. L. Selwyn, W. McKinnon, U. Von Sacken and C. Jones, *Solid State Ionics*, 1987, **22**, 337-344.
20. G. Du, Z. Guo, S. Wang, R. Zeng, Z. Chen and H. Liu, *Chem Commun (Camb)*, 2010, **46**, 1106-1108.
21. K. Chang and W. Chen, *Chem Commun (Camb)*, 2011, **47**, 4252-4254.
22. K. Chang and W. Chen, *ACS nano*, 2011, **5**, 4720-4728.
23. L. Yang, S. Wang, J. Mao, J. Deng, Q. Gao, Y. Tang and O. G. Schmidt, *Advanced materials*, 2013, **25**, 1180-1184.
24. X. Fang, X. Guo, Y. Mao, C. Hua, L. Shen, Y. Hu, Z. Wang, F. Wu and L. Chen, *Chem Asian J*, 2012, **7**, 1013-1017.
25. X. Fang, C. Hua, X. Guo, Y. Hu, Z. Wang, X. Gao, F. Wu, J. Wang and L. Chen, *Electrochimica Acta*, 2012, **81**, 155-160.
26. J. Xiao, X. Wang, X.-Q. Yang, S. Xun, G. Liu, P. K. Koech, J. Liu and J. P. Lemmon, *Advanced Functional Materials*, 2011, **21**, 2840-2846.
27. J. Xiao, D. Choi, L. Cosimbescu, P. Koech, J. Liu and J. P. Lemmon, *Chemistry of Materials*, 2010, **22**, 4522-4524.
28. J. Balach, T. Jaumann and L. Giebeler, *Energy Storage Materials*, 2017, DOI: 10.1016/j.ensm.2017.03.013.
29. Q. Wang and J. Li, *The Journal of Physical Chemistry C*, 2007, **111**, 1675-1682.
30. S. K. Das, R. Mallavajula, N. Jayaprakash and L. A. Archer, *Journal of Materials Chemistry*, 2012, **22**, 12988.
31. U. K. Sen, P. Johari, S. Basu, C. Nayak and S. Mitra, *Nanoscale*, 2014, **6**, 10243-10254.
32. G. Kresse and J. Furthmüller, *Physical review B*, 1996, **54**, 11169.
33. P. E. Blöchl, *Physical review B*, 1994, **50**, 17953.
34. J. Klimeš, D. R. Bowler and A. Michaelides, *Physical Review B*, 2011, **83**, 195131.
35. Y. Mao, H. Duan, B. Xu, L. Zhang, Y. Hu, C. Zhao, Z. Wang, L. Chen and Y. Yang, *Energy & Environmental Science*, 2012, **5**, 7950.
36. Y. Cheng, A. Nie, Q. Zhang, L.-Y. Gan, R. Shahbazian-Yassar and U. Schwingenschlogl, *ACS nano*, 2014, **8**, 11447-11453.
37. J. Wan, W. Bao, Y. Liu, J. Dai, F. Shen, L. Zhou, X. Cai, D. Urban, Y. Li, K. Jungjohann, M. S. Fuhrer and L. Hu, *Advanced Energy Materials*, 2015, **5**, 1401742.
38. F. Wang, R. Robert, N. A. Chernova, N. Pereira, F. Omenya, F. Badway, X. Hua, M. Ruotolo, R. Zhang, L. Wu, V. Volkov, D. Su, B. Key, M. S. Whittingham, C. P. Grey, G. G. Amatucci, Y. Zhu and J. Graetz, *Journal of the American Chemical Society*, 2011, **133**, 18828-18836.
39. F. Lin, D. Nordlund, T. C. Weng, Y. Zhu, C. Ban, R. M. Richards and H. L. Xin, *Nat Commun*, 2014, **5**, 3358.
40. P. Poizot, S. Laruelle, S. Grugeon, L. Dupont and J. Tarascon, *Nature*, 2000, **407**, 496-499.
41. Y. Yang, G. Zheng, S. Misra, J. Nelson, M. F. Toney and Y. Cui, *Journal of the American Chemical Society*, 2012, **134**, 15387-15394.

42. D. Yang, S. J. Sandoval, W. M. R. Divigalpitiya, J. C. Irwin and R. F. Frindt, *Physical Review B*, 1991, **43**, 12053-12056.
43. U. Gupta, B. S. Naidu, U. Maitra, A. Singh, S. N. Shirodkar, U. V. Waghmare and C. N. R. Rao, *APL Materials*, 2014, **2**, 092802.
44. M.-Y. Li, Y. Shi, C.-C. Cheng, L.-S. Lu, Y.-C. Lin, H.-L. Tang, M.-L. Tsai, C.-W. Chu, K.-H. Wei and J.-H. He, *Science*, 2015, **349**, 524-528.
45. H. Li, C. Tsai, A. L. Koh, L. Cai, A. W. Contryman, A. H. Fragapane, J. Zhao, H. S. Han, H. C. Manoharan, F. Abild-Pedersen, J. K. Norskov and X. Zheng, *Nature materials*, 2016, **15**, 364.
46. W. Divigalpitiya and X. Feng, *Chem. Mater*, 1994, **6**, 614-619.
47. H. Shu, F. Li, C. Hu, P. Liang, D. Cao and X. Chen, *Nanoscale*, 2016, **8**, 2918-2926.
48. D. Nasr Esfahani, O. Leenaerts, H. Sahin, B. Partoens and F. M. Peeters, *The Journal of Physical Chemistry C*, 2015, **119**, 10602-10609.
49. Z. Wu, G. Ouvrard, S. Lemaux, P. Moreau, P. Gressier, F. Lemoigno and J. Rouxel, *Physical review letters*, 1996, **77**, 2101.
50. L. Zhang, D. Sun, J. Feng, E. J. Cairns and J. Guo, *Nano Lett*, 2017, **17**, 5084-5091.
51. Y. Gorlin, A. Siebel, M. Piana, T. Huthwelker, H. Jha, G. Monsch, F. Kraus, H. A. Gasteiger and M. Tromp, *Journal of the Electrochemical Society*, 2015, **162**, A1146-A1155.
52. Z. W. Seh, Y. Sun, Q. Zhang and Y. Cui, *Chem. Soc. Rev.*, 2016, **45**, 5605-5634.
53. A. Manthiram, Y. Fu, S. H. Chung, C. Zu and Y. S. Su, *Chem Rev*, 2014, **114**, 11751-11787.
54. G. Zhou, H. Tian, Y. Jin, X. Tao, B. Liu, R. Zhang, Z. W. Seh, D. Zhuo, Y. Liu, J. Sun, J. Zhao, C. Zu, D. S. Wu, Q. Zhang and Y. Cui, *Proc Natl Acad Sci U S A*, 2017, DOI: 10.1073/pnas.1615837114.